Nano Research

Open Access

Research Article

Integrated multifunctional graphene aerogel combining wide temperature range sensing with high-efficiency electromagnetic shielding on a single platform

Fulei Lin[1], Yuxi Liu[1], Yunzhe Li[1], Dan Zhao[1], Huitao Yu[1,2,3], Yanan Li[1,2,3], and Ruiguang Xing[1,2,3] ✉

[1] *School of Materials Science and Engineering, Inner Mongolia University of Science and Technology, Baotou 014010, China*
[2] *Inner Mongolia Key Laboratory of Advanced Ceramic Material and Devices, Baotou 014010, China*
[3] *Key Laboratory of Green Extraction & Efficient Utilization of Light Rare-Earth Resources (Inner Mongolia University of Science and Technology), Ministry of Education, Baotou 014010, China*

Cite this article: *Nano Research*, **2026**, *19*, 94908789. https://doi.org/10.26599/NR.2026.94908789

ABSTRACT: The development of lightweight, multifunctional materials that integrate intelligent sensing with active protection is critically important for next-generation spacesuits and protective equipment operating in extreme environments. However, the integration of highly stable sensing performance with efficient electromagnetic interference (EMI) shielding over a broad temperature range remains a formidable challenge. Herein, through rational structural and compositional design, we fabricated a multifunctional composite aerogel composed of reduced graphene oxide, polyimide fibers, ethylenediamine tetramethylene phosphonic acid, and cobalt nitrate hexahydrate, enabling the seamless integration of wide temperature sensing and high-performance EMI shielding within a single material platform. The resulting aerogel exhibits stable and highly repeatable sensing behavior across a temperature range from −75 to 150 °C, as well as rapid response and recovery times (29 and 35 ms, respectively) under a 1 kg load and negligible performance degradation throughout 5000 loading–unloading cycles. Additionally, the composite shows excellent EMI shielding effectiveness, up to 48 dB in the 8–12 GHz. Thus, this work provides a viable strategy for the design of multifunctional materials capable of reliable operation under harsh conditions and offers new insights into the integrated development of intelligent sensing and protective systems for aerospace and extreme-environment applications.

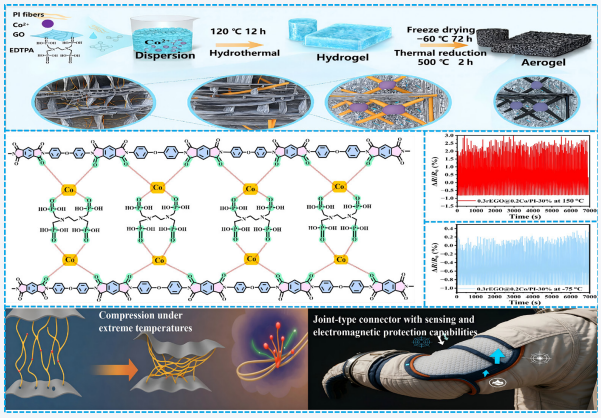

KEYWORDS: aerogel, wide-temperature-range sensing, electromagnetic shielding, graphene composite materials

1 Introduction

The extension of human exploration into extreme environments, including deep space and polar regions, increases the demand for high-performance intelligent protective materials capable of reliable operation under harsh conditions [1–4]. Spacesuits are the sole life-support and operational systems for astronauts in space; thus, their performance is critical to mission safety and execution efficiency [5, 6]. Conventional spacesuit architectures rely on the stacking of multiple independent functional layers, which leads to bulky structures, limited flexibility, and inherent challenges in integrating intelligent functionalities, such as real-time physiological monitoring, motion sensing, and adaptive environmental interaction [7]. Consequently, the development of lightweight [8], flexible [9], and multifunctional integrated material platforms that enable simultaneous self-sensing and active protection under extreme conditions [10]—such as wide temperature fluctuations, radiation exposure [11, 12], and mechanical stress—has emerged as a primary challenge in aerospace materials science and flexible electronics.

Among various materials, aerogels are considered an ideal carrier for multifunctional integration because of their ultralow density [13, 14], high porosity [15], large specific surface area [16], and adjustable physical and chemical properties [17, 18]. Among them, graphene-based aerogels have shown great potential in flexible

Received: March 7, 2026; **Revised:** April 14, 2026
Accepted: April 29, 2026

✉Address correspondence to xingrg06@163.com

sensing and electromagnetic shielding because of their excellent electrical conductivity, mechanical strength, and thermal stability [19–23]. For instance, Xie et al. obtained an independent partially reduced graphene aerogel through chemical reduction using ethylenediamine as the reducing agent, reporting extraordinary radiation response in a vacuum. Such good performance was mainly attributed to four structural features: extremely low thermal conductivity high porosity, ultralow density (4 mg/cm^3), and abundant functional groups [24]. Wei et al. prepared polypyrrole/reduced graphite oxide aerogel films using a simple sol–gel strategy followed by hydrothermal reduction. Assembled into a piezoresistive sensor, this aerogel exhibited a high sensitivity (0.9 kPa^{-1}) within a linear range of 0–1 kPa [25]. However, most studies still focus on the optimization of a single performance metric or only verify the functionality of the developed material near room temperature [26–29]. Its poor tensile performance limits its application in scalable electronic devices, intelligent soft robots, and aerospace [30–34]. The integration of thermal stability in a wide temperature range (especially ultralow and high temperatures), stable sensing, and efficient electromagnetic interference (EMI) shielding in a single aerogel system still faces many scientific challenges [35–37]. First, most polymeric matrices become brittle or soft at extreme temperatures, leading to structural failure. Second, the requirements for the microstructure of materials by the sensing mechanism and EMI shielding mechanism often differ, complicating their coordinated optimization [38, 39]. Finally, in a complex thermodynamic coupling environment, the interfacial stability and long-term cycling reliability between material components are difficult to guarantee [40–46].

2 Results and discussion

The proposed multifunctional ternary aerogel was rationally designed and fabricated via a simple one-step hydrothermal assembly strategy, as schematically illustrated in Fig. 1(a). Briefly, an aqueous dispersion containing graphene oxide (GO), alkali-treated hydrophilic polyimide (PI) fibers, cobalt nitrate hexahydrate ($Co(NO_3)_2{\cdot}6H_2O$), and EDTPA (EDTPA = ((ethane-1,2-diylbis(azanetriyl))tetrakis(methylene))tetrakis(phosphonic acid)) was hydrothermally treated at 120 °C. During this process, the *in situ* reduction of GO, coordination interactions between Co^{2+} and the phosphonate groups of EDTPA, and the simultaneous self-assembly of a three-dimensional (3D) interconnected network synergistically occurred. The resulting hydrogel was freeze-dried and subjected to stepwise thermal annealing, yielding a lightweight aerogel with a well-preserved hierarchical structure. As a result, the as-fabricated aerogel successfully integrates highly stable strain sensing over a broad temperature range (from −75 to 150 °C), with an EMI shielding effectiveness of up to 48 dB. The synergistic combination of mechanical robustness, environmental tolerance, and multifunctional integration endows this aerogel with promising potential for advanced applications, including aerospace smart skins, integrated protection for electronic devices, and sensing in extreme environments.

2.1 Microstructure of the graphene aerogel

Scanning and transmission electron microscopies were employed to reveal the microstructural evolution of the aerogel. Pristine GO exhibits a typical wrinkled, stacked-sheet morphology (Fig. 1(b)). After hydrothermal treatment, the layered structure of rGO partially diminishes (Fig. 1(c)). When graphene aerogel is added with a mass fraction of 30% PI fibers (rGO/PI-30%), its microstructure is significantly enhanced (Fig. 1(d)). We attributed this effect to the formation of abundant carboxyl and amino groups on the surface of PI fibers during alkaline hydrolysis. These groups form extensive hydrogen and ionic bonds with the oxygen-containing functional groups of graphene. Through these bonds, high-strength PI fibers interweave with graphene sheets to form a bridging structure that serves both as a flexible spacer and mechanical support. This structure effectively prevents pore collapse and imparts elasticity to the composite material. Additionally, after the addition of EDTPA, the aerogel exhibited a distinct porous structure (Fig. 1(e)), and the pore structure was refined upon the addition of $Co(NO_3)_2{\cdot}6H_2O$ (Fig. 1(f)). We attributed these effects to the synergy between two processes under hydrothermal conditions: EDTPA accelerates the reduction of GO to rGO and forms coordination bonds between its phosphine oxygen double bonds and Co ions, uniformly dispersing across the aerogel surface. This integration enables the formation of a unified system combining wide temperature range sensing, highly efficient electromagnetic shielding, and energy storage. Brunauer–Emmett–Teller (BET) testing revealed that the specific surface area of rGO is 5.4494 m^2/g. In contrast, the specific surface area of Sample 0.3rEGO@0.2Co/PI-30% was 19.6915 m^2/g. The pore sizes of Sample 0.3rEGO@0.2Co/PI-30% were primarily concentrated in the 5–20 nm range, with an average pore size of 17.4072 nm. This indicates that the aerogel has a mesoporous structure. When compressed, this mesoporous structure forms a large number of conductive network channels, thereby ensuring the output of sensing signals (Fig. S1(a) in the Electronic Supplementary Material (ESM)).

In addition, we measured the density of 0.3rEGO@0.2Co/PI-30%. First, we measured the volume of the aerogel using the Archimedes' principle and determined its mass using an electronic balance. To minimize errors, we performed three measurements on each sample and calculated the average. Finally, our calculations yielded a density of 0.0084925 g/cm^3 for the aerogel (Table S1 in the ESM).

TEM characterization revealed numerous dark nanoparticles uniformly anchored on the substrate surface without notable agglomeration, which were identified as Co-based complexes (Fig. 1(g)). To explicitly verify elemental distribution and coordination states, energy-dispersive X-ray spectroscopy was performed on the same region. The results (Figs. 1(h)–1(l)) indicate that C, N, O, P, and Co are uniformly distributed within the selected region.

Fourier transform infrared spectroscopy was employed to investigate chemical bonds within the aerogel. Results revealed characteristic O–H stretching vibration peaks at 3472 cm^{-1} for EDTPA, GO, and rGO. This indicates that the reduction degree of rGO is not high, and its surface contains abundant oxygen-containing functional groups (Fig. S2(a) in the ESM). With increasing EDTPA concentration, the characteristic peak at 3472 cm^{-1} in the spectrum of the aerogel considerably diminishes. This indicates that EDTPA promotes the reduction of GO to rGO (Fig. S2(b) in the ESM). With increasing $Co(NO_3)_2{\cdot}6H_2O$ content, the characteristic P=O bond peak at 1650 cm^{-1} in the aerogel is systematically redshifted from the higher wavenumber of the free state toward lower wavenumbers (Fig. 2(a)). The peak shape broadens or develops a shoulder peak, which was attributed to the

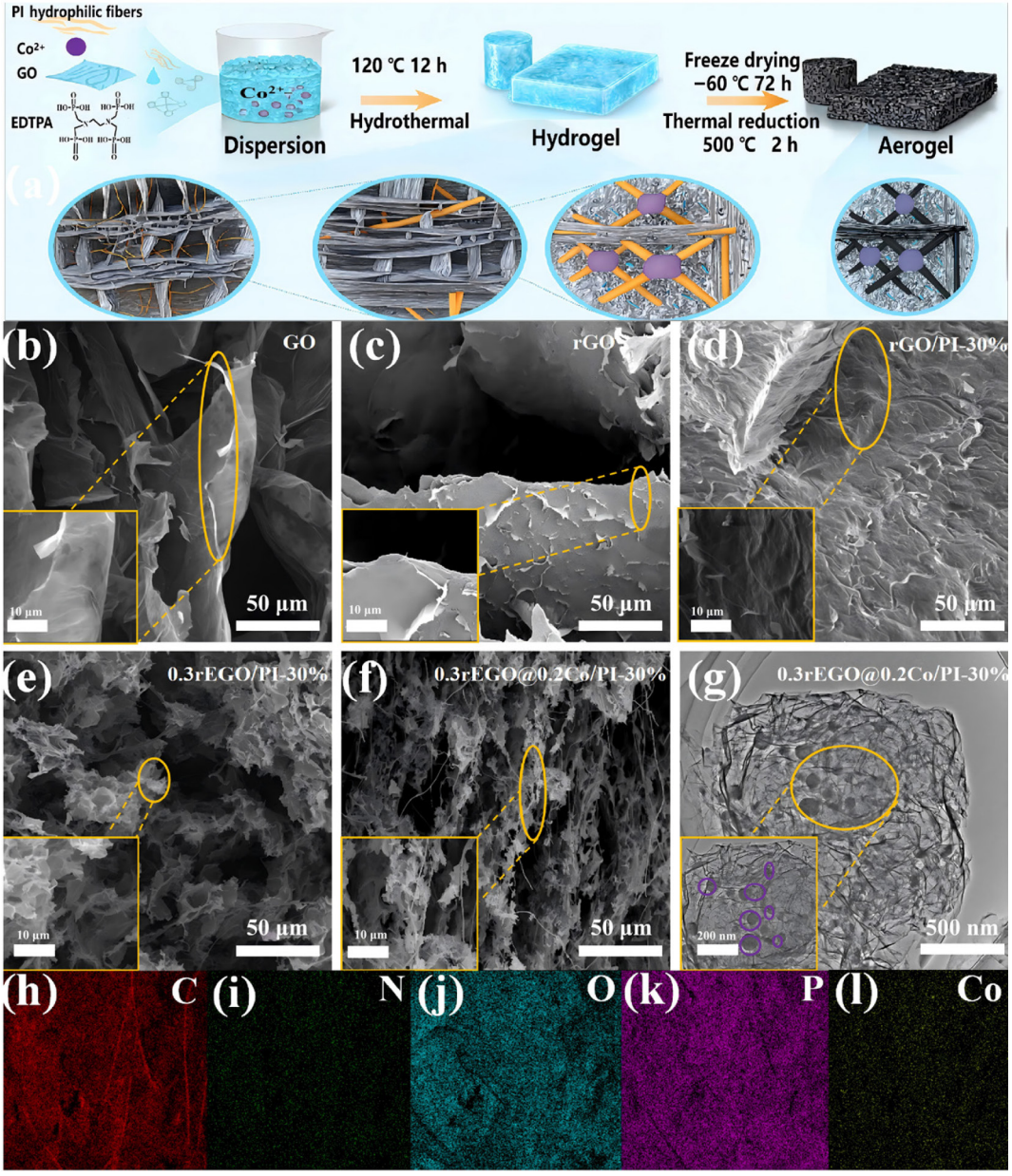

Figure 1 (a) Schematic diagram of the *y*rEGO/*z*Co/PI-*x*% preparation process. (b) SEM images of GO. (c) SEM images of rGO. (d) SEM images of rGO/PI-30%. (e) SEM images of 0.3rEGO/PI-30%. (f) SEM images of 0.3rEGO@0.2Co/PI-30%. (g) TEM images of 0.3rEGO@0.2Co/PI-30%. (h)–(l) EDS images of 0.3rEGO@0.2Co/PI-30%.

coordination of Co^{2+} with EDTPA, thereby resulting in the formation of P–O–Co chemical bonds. Furthermore, Raman and XRD tests demonstrated that the 0.3rEGO@0.2Co/PI-30% sample exhibits a more regular structure and fewer oxygen-containing functional groups compared to GO (Figs. S3(a) and S3(b) in the ESM).

Industrial X-ray computed tomography provides direct visual evidence of the evolution of hierarchical porous structures. The rGO aerogel exhibits a relatively uniform but incomplete pore network, indicating that pure graphene aerogel primarily comprises graphene flake structures (Fig. 2(b) and Fig. S4 in the ESM). Upon the incorporation of PI fibers, the framework becomes considerably more robust and interconnected, with PI fibers uniformly distributed between graphene flakes (Fig. 2(c) and Fig. S5 in the ESM). This occurs because PI fibers function both as reinforcing spacers and crosslinking nodes, thereby forming finer primary pores. In the 0.3rEGO/PI-30% sample, this trend is further amplified because EDTPA acts as a reducing agent, leading to a higher degree of GO reduction (Fig. 2(d) and Fig. S6 in the ESM). Most notably, the introduction of Co ions (0.3rEGO@0.2Co/PI-30%) resulted in a more pronounced and clearly defined porous structure, with Co ions uniformly dispersed throughout the aerogel (Fig. 2(e) and Fig. S7 in the ESM).

A schematic in Fig. 2(f) shows the chemical transformation that PI fibers undergo during composite fabrication. Through hydrolysis in an alkaline solution, PI fibers can be effectively dispersed in water. Under hydrothermal conditions at 120 °C, the reduction of GO proceeds concurrently with the initial imidization of PI fibers, enabling the self-assembly of PI fibers within the rGO pore structure. During thermal reduction at 500 °C, residual amine and

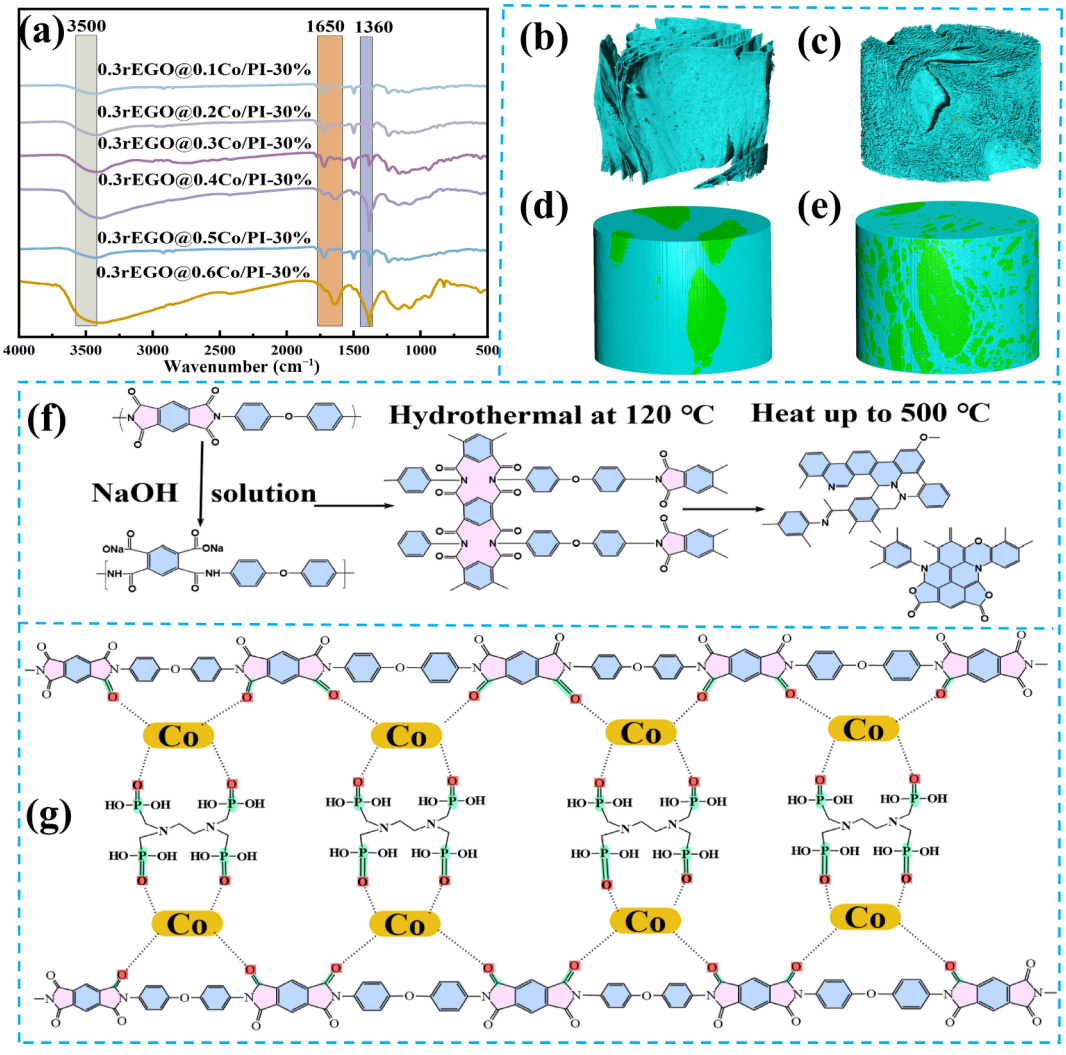

Figure 2 (a) Infrared spectra of aerogels with different $Co(NO_3)_2{\cdot}6H_2O$ ratios. Industrial X-ray computed tomography (CT) images of (b) rGO, (c) rGO/PI-30%, (d) 0.3rEGO/PI-30%, and (e) 0.3rEGO@0.2Co/PI-30%. (f) Schematic diagram of the hydrolysis process of PI fibers. (g) Schematic diagram of Co^{2+} coordination.

carboxyl groups in PI can undergo condensation reactions with oxygen-containing functional groups (e.g., –COOH, –OH) on graphene sheets or with each other, re-forming amide or imide bonds. This reaction effectively crosslinks hydrolyzed PI fiber fragments with the graphene network, forming a scaffold integrated into a 3D framework through covalent bonds, imparting mechanical strength to the aerogel.

Figure 2(g) shows the chemical structure of Co-ion coordination. Cobalt ions are physically encapsulated and chemically anchored via coordinate bonds. This multidentate coordination forms stable composite nodes at the interface between rGO and PI. These nodes not only enhance structural integrity but also introduce magnetic moments and additional dipole polarization centers, which are crucial for improving the electromagnetic wave dissipation capability of the final aerogel.

2.2 Mechanism of superelasticity in graphene aerogels

To investigate the crosslinking mechanism during the formation of aerogel 0.3rEGO@0.2Co/PI-30%, X-ray photoelectron spectroscopy was conducted. The resulting spectrum (Fig. 3(a)) confirms the successful incorporation of all designed components into the composite aerogel, revealing the elemental composition of the ternary composite system [47]. More importantly, a characteristic P–O–Co peak at 531.5 eV is observed in the high-resolution O 1s spectrum (Fig. 3(b)), indicating the successful coordination of Co ions. Furthermore, the high-resolution Co 2p, C, N and P spectra (Fig. 3(c) and Fig. S8 in the ESM) provides deeper insights into the chemical state of Co. This spectrum was resolved into two primary spin-orbit doublets. A prominent satellite peak resides on the high-binding-energy side of the Co 2p main peak, a satellite feature that is the unambiguous fingerprint of Co^{2+}. The binding energy of the Co 2p peak is approximately 781.1 eV, which is higher than that of pristine CoO (approximately 780 eV). This positive shift strongly indicates that Co^{2+} coordinates with highly electronegative oxygen atoms from the EDTPA phosphate group, forming stable P–O–Co coordination structures. This molecular-level design is crucial for the introduction of dipole polarization and magnetic loss centers, which underpin the efficient microwave absorption of the material and its sensitive dielectric response.

As shown in Figs. 3(d)–3(f), progressive compression tests were performed on sample 0.3rEGO@0.2Co/PI-30% at –75, 25, and 150 °C. The results indicate that at –75 °C, the stresses at 50%, 75%, and 90% strains are 36.39, 110.37, and 120.07 kPa, respectively. At 25 °C, the stresses at 50%, 75%, and 90% strains are 39.95, 120.09,

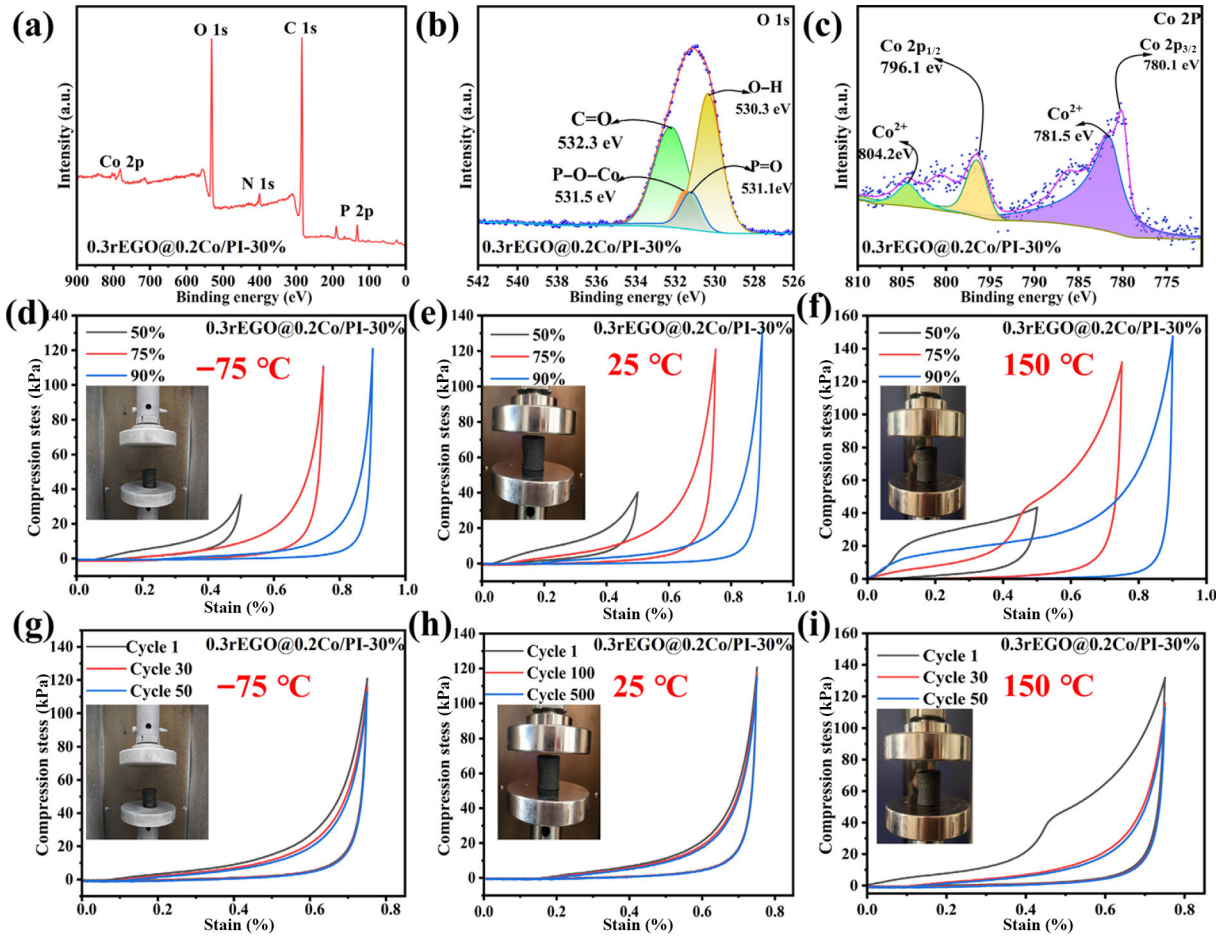

Figure 3 (a)–(c) X-ray photoelectron spectrum of sample 0.3rEGO@0.2Co/PI-30%. (d)–(f) Stress–strain curves of sample 0.3rEGO@0.2Co/PI-30% under stepwise compression at cryogenic, room, and elevated temperatures. (g)–(i) Stress–strain curves of sample 0.3rEGO@0.2Co/PI-30% under cyclic compression at 75% strain at cryogenic, room, and elevated temperatures.

and 131.13 kPa, respectively. At 150 °C, the stresses at 50%, 75%, and 90% strains are 43.59, 131.83, and 147.41 kPa, respectively. This indicates that within a small range of compressive strain, stress slowly increases in a linear manner, corresponding to elastic deformation of the spider web–like cell walls. As compressive strain increases, stress sharply rises because of the contraction of the porous structure, marking the transition from the linear elastic region to the densification zone. Notably, even after enduring 90% strain at extreme temperatures, stress can recover to its initial level, highlighting the exceptional ability of the material to maintain structural integrity during high deformation. We primarily attributed this behavior to two synergistic mechanisms. First, the entropic elastic contribution to modulus from PI fibers acting as the reinforcing phase, which increases with temperature in their highly elastic state, exemplifying rubber elasticity theory. Second, the removal of interfacial water between components at elevated temperatures, coupled with enhanced interfacial prestress owing to thermal expansion mismatch, collectively induces a thermosetting effect [48]. This phenomenon indicates that our material does not passively endure extremely high temperatures but actively maintains and even increases its structural rigidity and stability under such conditions. This provides a robust mechanical foundation for sustaining reliable sensing and protective functions in applications characterized by wide temperature fluctuations.

As shown in Figs. 3(g)–3(i), cyclic compression tests were conducted on sample 0.3rEGO@0.2Co/PI-30% at 75% strain and temperatures of −75, 25, and 150 °C. The aerogel sample underwent 50 compression cycles at −75 °C (Fig. 3(g)). After 30 and 50 cycles, the maximum compressive stresses were 115.09 and 111.19 kPa, respectively, indicating that the material retained 95.13% and 91.92% of the initial stress (120.97 kPa). As shown in Fig. 3(h), after 100 and 500 cycles at 25 °C, the maximum compressive stresses were 114.87 and 110.96 kPa, respectively, retaining 95.68% and 92.43% of the initial stress (120.05 kPa). As shown in Fig. 3(i) after 30 and 50 cycles at 150 °C, the maximum compressive stresses were 115.51 and 109.62 kPa, respectively, retaining 88.20% and 83.70% of the initial stress (130.96 kPa). These results indicate that PI fibers, serving as the supporting skeleton, maintain excellent elasticity and strength across a wide temperature range, with their covalent bond structure remaining resistant to fracture under cyclic loading. Furthermore, the P–O–Co coordination bonds act as dynamic yet stable crosslinking points, enabling the network to dissipate energy during deformation while preventing permanent structural slip.

To further evaluate the superelasticity of 0.3rEGO@0.2Co/PI-30% under extreme conditions, first, the aerogel was compressed to a height of 1 cm using a weight of 1 kg. Upon the removal of the weight, the aerogel rapidly recovered to its initial height of 3 cm. Second, the aerogel sample was immersed in liquid nitrogen for 20 min, followed by cyclic compression testing in liquid nitrogen.

The aerogel exhibited negligible deformation loss, confirming its superelasticity even at extremely low temperatures. Beyond external compression forces, extreme compression folding can be achieved through vacuum extraction. After being subjected to vacuum using a vacuum sealer, repeated folding and unfolding, the surface of the aerogel remained smooth and free of wrinkles (Figs. S9 and S10 in the ESM). This indicates the promising potential of the aerogel as a wearable sensor for human use under extreme environmental conditions.

2.3 Sensing properties of the prepared aerogel

To investigate the effects of different components on the sensing performance of this aerogel, we conducted the following experiments. As shown in Figs. 4(a)–4(c), the resistive sensing signal of the aerogel first increased and then decreased with the addition of PI fibers, EDTPA, and $Co(NO_3)_2{\cdot}6H_2O$. This occurs because PI fibers, acting as insulators, can form a stable 3D framework when added in appropriate amounts (e.g., 30%). This framework prevents graphene agglomeration, enabling its uniform dispersion and creating more effective conductive pathways [49]. At the same time, EDTPA, as a multifunctional molecule, serves as a "bridge". It enhances interfacial connections between rGO, PI, and Co^{2+} species through chemical and hydrogen bonds, thereby reducing contact resistance and optimizing electron transport pathways. The introduction of Co^{2+} exerts a dual effect. First, as a dopant, it introduces defects or charges between rGO layers, enhancing intrinsic conductivity. Second, it coordinates with oxygen-containing functional groups, further strengthening crosslinking between components. However, excessive PI dilutes the concentration of conductive fillers and makes conductive pathways sparse or even interrupted. This degradation in network integrity leads to a sluggish response to stimuli. Excessive EDTPA content induces overcrosslinking, rendering the material excessively hard and brittle, depriving it of microdeformation capability essential for flexible sensing. More critically, excess Co^{2+} may form insulating metal-oxide (CoO) aggregates that overcoat rGO sheets,

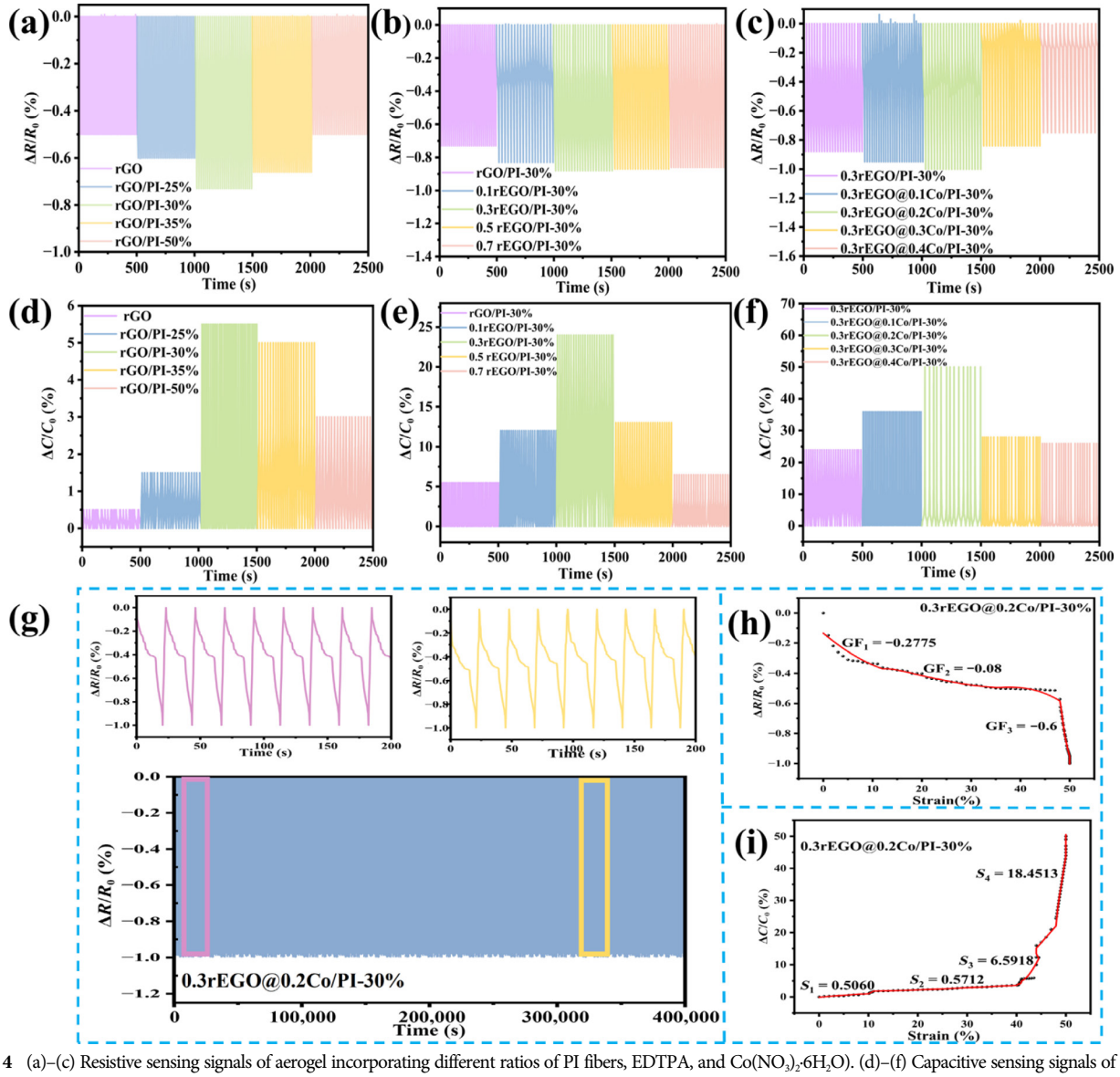

Figure 4 (a)–(c) Resistive sensing signals of aerogel incorporating different ratios of PI fibers, EDTPA, and $Co(NO_3)_2{\cdot}6H_2O$). (d)–(f) Capacitive sensing signals of aerogel incorporating different ratios of PI fibers, EDTPA, and $Co(NO_3)_2{\cdot}6H_2O$). (g) Sensing signal of sample 0.3rEGO@0.2Co/PI-30% after 5000 cycles. (h) Resistive sensitivity of sample 0.3rEGO@0.2Co/PI-30%. (i) Capacitance sensitivity of 0.3rEGO@0.2Co/PI-30%.

obstructing electron transport. Thus, the optimal combination of these three components results in the construction of a highly interconnected and sensitive conductive network. When subjected to external stimuli, such as strain or pressure, the internal connection points or tunnel resistances within the network considerably change, generating strong resistive response signals.

Although capacitive sensing signals initially increased and then decreased with the incorporation of PI fibers, EDTPA, and $Co(NO_3)_2{\cdot}6H_2O$ into the aerogel (Figs. 4(d)–4(f)), which was primarily attributed to changes in the dielectric constant of the material. In porous aerogels, capacitive response is primarily related to interfacial polarization and ion migration [50]. EDTPA molecules possess polar groups, whereas Co^{2+} is a charged ion. Thus, their incorporation at appropriate levels creates abundant interfacial polarization sites at the boundary between the insulating PI matrix and conductive rGO. At an appropriate ratio, PI fibers provide the porous structure, rGO serves as the electrode, and EDTPA and Co^{2+} jointly function as an excellent dielectric layer. This configuration enables effective changes in the microcapacitor structure under pressure or deformation, generating notable capacitance variation signals. Furthermore, the aerogel exhibits virtually no signal decay after 5000 cycles (Fig. 4(g)), reflecting its multilevel structural stability and robust interfacial integrity. The sensitivity factor (GF), a metric evaluating the sensitivity of the aerogel, was calculated using Eqs. (S1) and (S2) in the ESM, derived from the slopes of the relative capacitance ($\Delta C/C_0$) and resistance change rate ($\Delta R/R_0$) curves versus strain. As compressive strain increases, $\Delta C/C_0$ increases while $\Delta R/R_0$ decreases (Figs. 4(h) and 4(i)). These results were attributed to the increased heterogeneity of the aerogel matrix and pore desification during compression, which reduces the length of conductive pathways and consequently lowers the relative resistance under applied pressure.

2.4 Flexible sensing performance of the aerogel in human wearable devices

Figure 5 presents the flexible sensing performance of the prepared aerogel and reveals its intrinsic working mechanism. The results indicate that this material exhibits high sensitivity, rapid response, and excellent stability when monitoring human movements at different scales. Its dual-mode resistive and capacitive sensing capabilities make it suitable for use in complex real-world scenarios. Finger bending (Figs. 5(a) and 5(d)) and elbow flexion (Figs. 5(b) and 5(e)) are medium-to-high frequency, medium-to-low strain movements. Both resistive and capacitive signals clearly and reproducibly respond to the initiation and termination of these actions. Notably, the baseline of the resistive signal fully recovers after the action, whereas the capacitive signal exhibits a slight baseline drift after multiple cycles. This reflects the fundamental

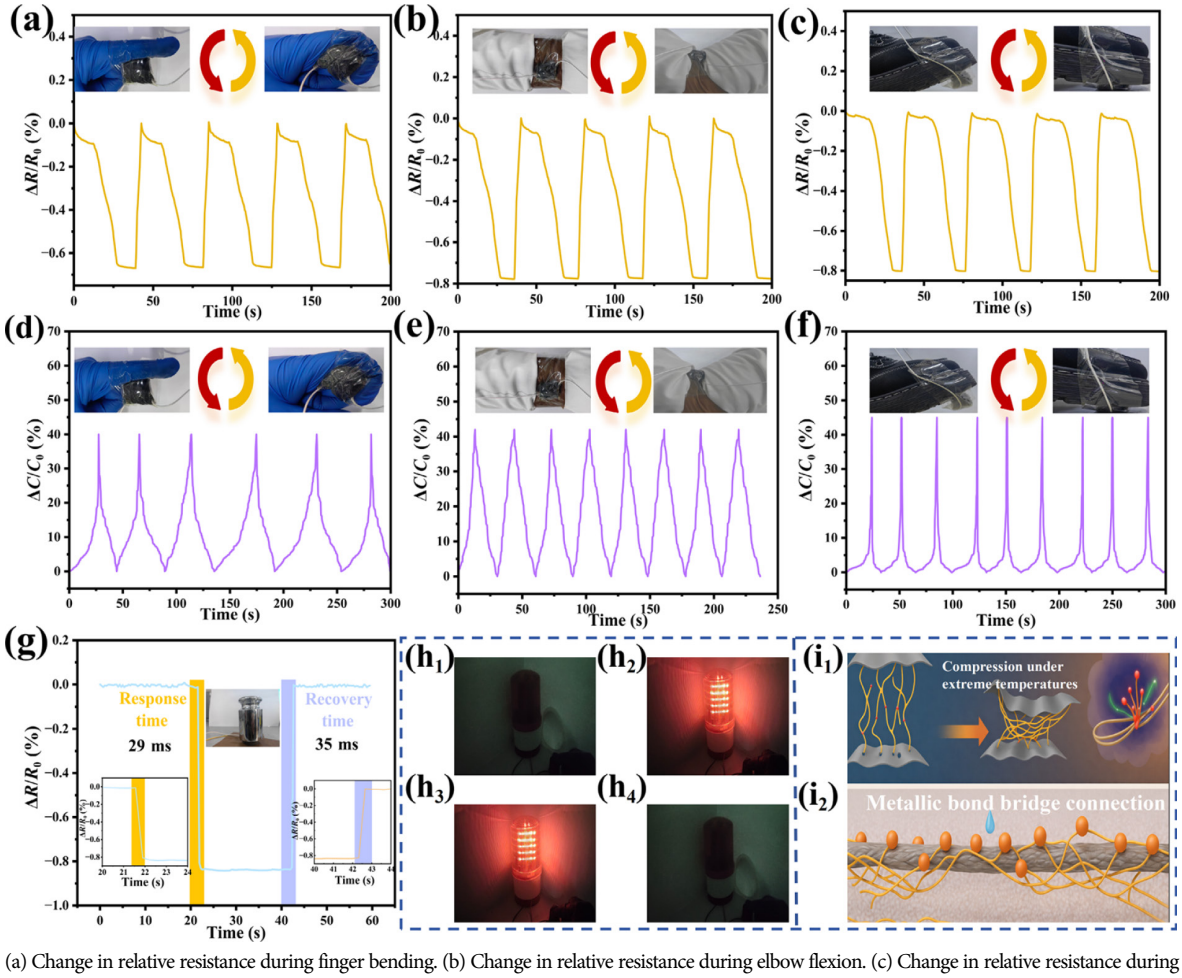

Figure 5 (a) Change in relative resistance during finger bending. (b) Change in relative resistance during elbow flexion. (c) Change in relative resistance during simulated walking. (d) Change in relative capacitance during finger bending. (e) Change in relative capacitance during elbow flexion. (f) Change in relative capacitance during simulated walking. (g) Response and recovery time under 1 kg weight load. (h_1)–(h_4) Comparison of electrical conductivity at different compression levels. (i_1) and (i_2) Schematic diagram of the aerogel sensing mechanism.

difference between the two sensing mechanisms: resistive changes primarily depend on the reversible deformation of the conductive network, whereas capacitive changes involve more complex interfacial charge rearrangement and accumulation, whose recovery may be slightly slower [51]. Walking motion in this scenario mimics low-frequency, large strain cyclic stress (Figs. 5(c) and 5(f)). Capacitive signals show notable advantages here, exhibiting a change magnitude ($\Delta C/C_0$ reaching approximately −45%) far exceeding that of resistive signals ($\Delta R/R_0$ around 0.8%). This was primarily attributed to the considerable compression of the porous structure of the aerogel under high pressure. This compression process significantly reduces the spacing between the electrodes (conductive rGO layers), thereby forming a microcapacitor structure and decreasing the effective thickness of the dielectric layer, which is the primary reason for the significant change in capacitance. In addition, periodic low-frequency, high-strain pressure enhances ion migration (of EDTPA and Co species) and interfacial polarization effects. These factors also contribute to changes in capacitance, though they are not the primary causes. At the same time, the resistive network may approach its reconstruction limit under large strain, resulting in a relatively saturated rate of change. This further indicates the dual-mode resistive–capacitive sensing capability of the aerogel. The resistive mode, with its fast response and stable baseline, is better suited for monitoring rapid, subtle deformations. The capacitive mode, however, exhibits exceptional sensitivity to slow, large-amplitude pressure changes (e.g., gait, sitting/lying postures), offering higher sensitivity. This complementarity greatly expands the application scope of the material in wearable health monitoring.

Figure 5(g) presents the dynamic response of the material under a 1 kg weight. The measured response time is 29 ms, with a recovery time of 35 ms. Such a rapid response was attributed to the highly porous and elastic 3D structure of the aerogel, where the PI fiber skeleton and the open pores of the aerogel enable rapid pressure transmission and induce instantaneous elastic deformation of the structure. The robust conductive/dielectric network formed by strong P–O–Co bonds ensures that electrical signals synchronously follow mechanical deformation without significant hysteresis. This performance metric indicates the capability of the sensor to capture dynamic mechanical stimuli in real-time with high accuracy, meeting demands for rapid motion monitoring. Figure 5(h_1)–5(h_4) visually presents the tunable conductivity of the material through schematics of conductive pathways under varying compression levels. Although rGO itself forms a conductive network in the uncompressed state, some connections remain point or tunneling contacts, resulting in relatively high resistance. As compression increases, the pores in the aerogel are compressed, increasing the number of contact points and contact area between conductive fillers, even forming new conductive pathways. This leads to a continuous decrease in the overall resistance of the material, ultimately activating the alarm. A schematic in Fig. 5(i_1) comprehensively summarizes the microscopic origin of these properties.

When the aerogel is compressed, its internal conductive network consists of rGO and Co nanoparticles/clusters as shown in Fig. 5(i_2). This alters the distance between conductive particles, affecting tunneling resistance, and causes conductive pathways to connect or disconnect. These changes collectively induce sensitive changes in macroscopic resistance. Furthermore, the prepared aerogel can be conceptualized as a sponge filled with microcapacitors. Each microcapacitor features rGO sheets as electrodes and a dielectric layer composed of pore regions rich in polar molecules (PI, EDTPA) and Co^{2+}. External pressure not only reduces electrode spacing and compresses the dielectric layer—altering its effective permittivity—but also facilitates ion migration. The ingenuity of this material lies in its PI fiber framework providing mechanical support and compressibility, rGO delivering conductivity and electrode foundations, and EDTPA and Co^{2+} considerably improving dielectric properties and interfacial polarization capability. This enables the simultaneous optimization of resistive and capacitive signals [52].

2.5 Sensing performance and thermal stability in extreme environments as well as application potential of the aerogel in spacesuits

Figures 6(a) and 6(b) show the real-time sensing signals of the material at ultralow (−75 °C) and high (150 °C) temperatures, respectively. As shown in Fig. 6(a), the aerogel maintains stable and repeatable sensing signals even at extremely low temperatures. This stability was primarily attributed to the exceptional low-temperature toughness of the PI fiber framework. Its molecular chains resist embrittlement at cryogenic temperatures, ensuring the integrity of the 3D network structure of the aerogel. Furthermore, carrier transport within the conductive network formed by rGO and Co^{2+} exhibits low-temperature dependency. Protected by the strong P–O–Co interfacial bonds, the network remains resilient against thermal stress–induced failure. This performance indicates the direct applicability of the fabricated sensor in ultralow-temperature environments, such as deep space shadow zones, lunar night, or Martian polar regions, for monitoring astronaut joint movements or spacesuit pressure conditions. As shown in Fig. 6(b), the sensing signal remains stable at 150 °C, without any notable drift or attenuation. This is because PI is a well-known high-temperature polymer with a decomposition temperature far exceeding 150 °C. Graphene layers form a thermal barrier around PI fibers, blocking the rapid transfer of heat and decomposition products, thereby delaying the thermal decomposition of PI fibers. The stable coordination structure formed between Co^{2+} and EDTPA acts as a chemical crosslinking point, tightly bonding graphene layers to PI fibers. This reinforced interface inhibits the slippage of polymer chains and the escape of volatile molecules during heating. In the late stage of high-temperature pyrolysis, interconnected carbon phases formed from rGO and carbonized PI establish a continuous, robust conductive carbon network, providing structural support to maintain the overall integrity of the material. Figures 6(c) and 6(d) show schematics of the integrated application of this aerogel in spacesuits. The aerogel film can be cut and embedded in joint areas (e.g., elbows and knees), pressure layers of the torso, or glove fingertips. It can simultaneously or selectively monitor joint bending angles and movement frequencies through changes in resistance/capacitance (corresponding to human motion monitoring data in Figs. 5(a)–5(f). Compared with traditional rigid, single-function sensors, this lightweight, flexible, and multifunctional integrated aerogel sensor considerably improves the comfort, mobility, and intelligence of the spacesuit, enabling real-time (Fig. S11 in the ESM), imperceptible monitoring of human condition and environmental interactions [53].

Additionally, Figs. 6(e)–6(g) present another key function of this aerogel: EMI shielding. The curve in Fig. 6(e) indicates highly effective EMI shielding performance of up to 48 dB in the

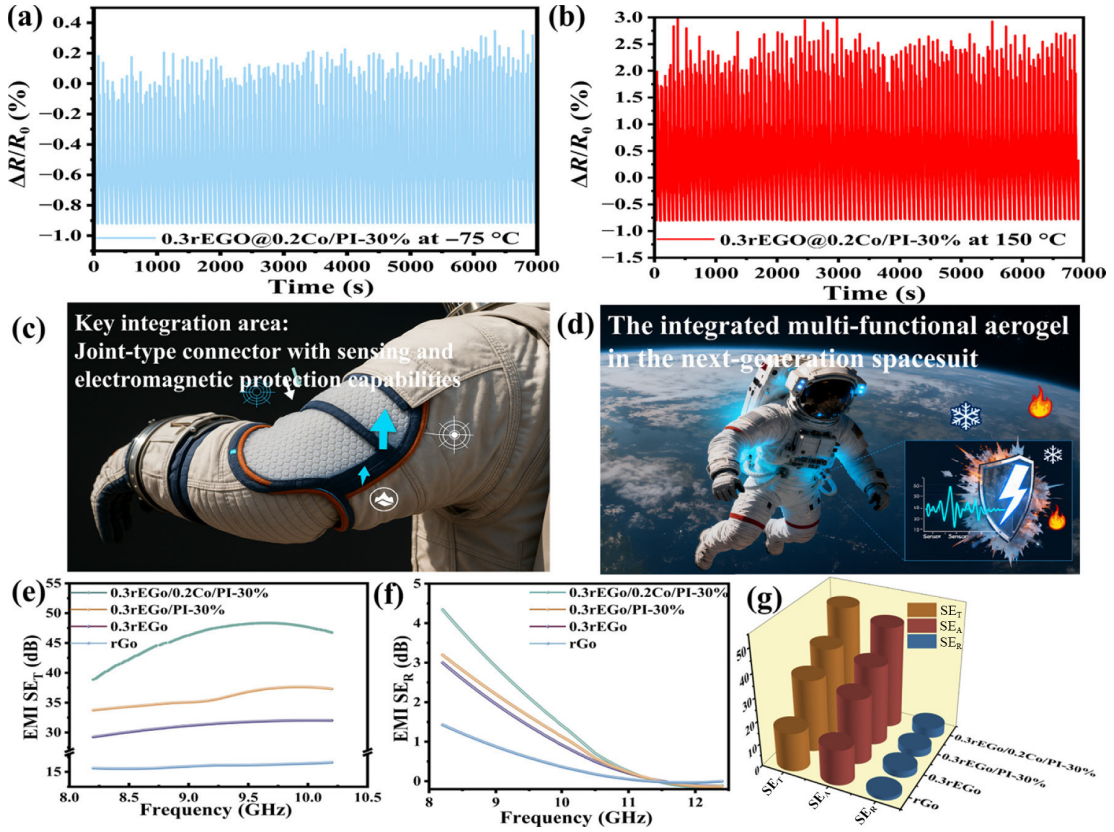

Figure 6 (a) Sensing signal of aerogel 0.3rEGO@0.2Co/PI-30% at −75 °C. (b) Sensing signal of aerogel 0.3rEGO@0.2Co/PI-30% at 150 °C. (c) and (d) Application of aerogels in wearable spacesuit sensors. (e)–(g) Electromagnetic shielding performance of aerogels.

8–12 GHz band. Specifically, the reflectance coefficient (R) is approximately 0.375, the absorption coefficient (A) is approximately 0.605, and the transmittance coefficient (T) is approximately 0.02. This indicates that absorption is the primary shielding mechanism for this aerogel (Fig. S12 in the ESM). This means that the prepared aerogel can block over 99.9% of incident electromagnetic waves, meeting commercial and military standards. To further illustrate the EMI shielding performance of the aerogel, we measured radiation levels during mobile phone charging before and after aerogel placement. Without the aerogel, low-frequency radiation as high as 284 V/m was detected, whereas radiation levels dropped to 0.09 V/m after aerogel placement (Fig. S13 in the ESM). This reduction was attributed to the formation of conductive pathways in the 3D continuous rGO network, which induce conductive losses. Concurrently, EDTPA molecules, Co^{2+} ions, and the abundant interfaces they form with rGO/PI generate dipole and interface polarization under alternating electromagnetic fields, dissipating electromagnetic energy. The multilevel pore structure of the material enables multiple reflections and scattering of electromagnetic waves, extending their propagation path and enhancing dissipation. This enables spacesuits incorporating the aerogel to not only sense physical signals but also actively protect astronauts and internal precision electronics from EMI and potential information leakage risks, integrating sensing and protective functions [54].

3 Conclusion

Herein, a novel graphene-based aerogel composite was prepared through an ingenious multicomponent synergistic design strategy, integrating wide temperature range superelasticity, high sensitivity dual-mode sensing, and efficient EMI shielding in a single material. Systematic experimental characterization and performance tests indicated that the optimized 0.3rEGO@0.2Co/PI-30% aerogel exhibits outstanding superelasticity and fatigue resistance across a temperature range from −75 to 150 °C, attributed to the synergistic interaction between the PI framework and P–O–Co dynamic coordination bonds. This aerogel exhibited dual-mode sensing capabilities for both resistance and capacitance, considerably expanding application scenarios for wearable devices. Under 1kg pressure, its response and recovery times were 29 and 35 ms, respectively, with no signal attenuation after 5000 cycles. Sensing functionality remained stable at −75 and 150 °C, with high thermal decomposition temperature and char yield. Its intrinsic thermal stability ensures reliable operation under thermal shock conditions. Furthermore, within the 8–12 GHz frequency band, the material showed a maximum EMI shielding effectiveness of 48 dB. In summary, this work not only elucidates the rational construction principles and synergistic mechanisms of high-performance multifunctional aerogels across the molecular, microscopic, and macroscopic scales but also overcomes the limitations of single-function traditional materials. It provides a feasible material prototype and design paradigm for the development of next-generation intelligent protection systems (advanced spacesuits integrating self-sensing, adaptive, and active electromagnetic protection capabilities) for frontier applications such as deep space exploration and extreme-environment operations. For example, the aerogel can be cut into small pieces and placed on the fingers, arms, and knees of a spacesuit. This allows for the monitoring of the astronaut's physical health through their daily activities in space. Consequently, the immense potential of this aerogel for functional integration on a single platform offers significant prospects for

advancing the development of flexible electronics, smart protection, and advanced composite materials.

Electronic Supplementary Material: Supplementary materials (including experimental details such as the preparation of graphene oxide, the preparation of graphene aerogel, strain sensor testing methods, sensor sensitivity equations, and *R* and *T* parameters, as well as photographs of the results) are available in the online version of this article at https://doi.org/10.26599/NR.2026.94908789.

Data availability

All data needed to support the conclusions in the paper are presented in the manuscript and the Electronic Supplementary Material. Additional data related to this paper may be requested from the corresponding author upon request.

Acknowledgements

This study was supported by the Natural Science Foundation of Inner Mongolia (Nos. 2024LHMS05043 and 2025LHMS05038).

Declaration of competing interest

The authors declare that they have no known competing financial interests or personal relationships that could have appeared to influence the work reported in this paper.

Author contribution statement

F. L. L.: Writing – original draft, investigation, data curation. Y. X. L.: Investigation. Y. Z. L.: Methodology, investigation. D. Z.: Validation, methodology. H. T. Y.: Supervision. Y. N. L.: Supervision, data curation. R. G. X.: Writing – review & editing, supervision, conceptualization.

Use of AI statement

None.

References

[1] Yu, C.; Guo, J. H.; Lv, S. X.; Jiang, X. H. Modified zirconia fiber/reduced graphene oxide composite aerogels with exceptional mechanical and microwave absorption properties for harsh-environment applications. *Chem. Eng. J.* **2023**, *468*, 143850.

[2] Yang, D.; Nam, H. K.; Lee, Y.; Kwon, S.; Lee, J.; Yoon, H.; Kim, Y. J. Laser-induced graphene smart textiles for future space suits and telescopes. *Adv. Funct. Mater.* **2025**, *35*, 2411257.

[3] Tao, G. M.; Wu, J. W.; Zhu, M. F. Encapsulated aerogel fiber mimicking the "core–shell" structure of polar bear hair for thermal insulation. *Adv. Fiber Mater.* **2024**, *6*, 329–331.

[4] Cheng, Y. J.; Cheng, H. L.; Gao, J.; Xue, Y. J.; Han, G. J.; Zhou, B.; Liu, C. T.; Feng, Y. Z.; Shen, C. Y. Air-drying for rapid manufacture of flexible aramid nanofiber aerogel fibers with robust mechanical properties and thermal insulation in harsh environments. *Small* **2025**, *21*, 2409408.

[5] Yang, J.; Li, Y.; Zheng, Y. Y.; Xu, Y. M.; Zheng, Z. K.; Chen, X. D.; Liu, W. Versatile aerogels for sensors. *Small* **2019**, *15*, 1902826.

[6] Prakash, P.; Weerasinghe, J.; Levchenko, I.; Prasad, K.; Alexander, K. Polyimide nanocomposites for next generation spacesuits. *Mater. Horiz.* **2025**, *12*, 3633–3666.

[7] Ryu, K. H.; Kang, M.; Kim, J.; You, N. H.; Jang, S. G.; Jeong, K. U.; Ahn, S.; Kim, D. E. Y. Spacesuit textiles from extreme fabric materials: Aromatic amide polymer and boron nitride nanotube composite fiber for neutron shielding and thermal management. *Adv. Fiber Mater.* **2024**, *6*, 1509–1520.

[8] Yuan, Q.; Yan, L. W.; Tian, J. F.; Ding, W. Y.; Heng, Z. G.; Liang, M.; Chen, Y.; Zou, H. W. *In situ* ceramization of nanoscale interface enables aerogel with thermal protection at 1950 °C. *ACS Nano* **2024**, *18*, 3520–3530.

[9] Yang, C. H.; He, P.; Wang, W. Y.; Han, R.; Zhang, H. T.; Nie, M.; Liu, Y. Layer-by-layer assembled aramid nanofiber/MXene aerogel: Exceptional resistance to extreme temperatures and robust anisotropy for advanced applications. *Compos. Sci. Technol.* **2024**, *257*, 110833.

[10] Wang, S.; Ding, R. D.; Liang, G. Q.; Zhang, W.; Yang, F. J.; Tian, Y. C.; Yu, J. Y.; Zhang, S. C.; Ding, B. Direct synthesis of polyimide curly nanofibrous aerogels for high-performance thermal insulation under extreme temperature. *Adv. Mater.* **2024**, *36*, 2313444.

[11] Dai, X. Y.; Liang, Q. H.; Zhao, Z. H.; Wu, Y. H.; Yang, J. K.; Han, J. X.; Cao, Y. J.; Wang, Y. P.; Li, C. H.; Zhong, A. H. et al. Self-powered sensors for flexible electronic skins capable of self-healing under multiple extreme environments. *Nano Energy* **2024**, *121*, 109239.

[12] Yue, Y. M.; Tang, Y.; Wang, Q.; Xiao, W. J.; Liu, J.; Wang, J. X.; Chen, M.; Wu, G. X.; Su, B. Active perception in non-visual recognition environments by stretchable tentacle sensor arrays. *ACS Appl. Mater. Interfaces* **2022**, *14*, 26913–26922.

[13] Qian, F.; Troksa, A.; Fears, T. M.; Nielsen, M. H.; Nelson, A. J.; Baumann, T. F.; Kucheyev, S. O.; Han, T. Y. J.; Bagge-Hansen, M. Gold aerogel monoliths with tunable ultralow densities. *Nano Lett.* **2020**, *20*, 131–135.

[14] Liu, S.; Yue, X. Y.; Liu, S.; Yang, W. K.; Liu, H.; Liu, C. T.; Shen, C. Y. Deep learning-assisted tactile sensing platform for efficient object classification and password recognition. *J. Mater. Sci. Technol.* **2026**, *260*, 241–252.

[15] Dong, Y.; Hao, L.; Shi, Z. D.; Fang, K.; Yu, H.; Zang, G. H.; Fan, T.; Han, C. H. Solasonine induces apoptosis and inhibits proliferation of bladder cancer cells by suppressing NRP1 expression. *J. Oncol.* **2022**, *2022*, 7261486.

[16] Du, R.; Wang, J. Y.; Wang, Y.; Hübner, R.; Fan, X. L.; Senkovska, I.; Hu, Y.; Kaskel, S.; Eychmüller, A. Unveiling reductant chemistry in fabricating noble metal aerogels for superior oxygen evolution and ethanol oxidation. *Nat. Commun.* **2020**, *11*, 1590.

[17] Maleki, H. Recent advances in aerogels for environmental remediation applications: A review. *Chem. Eng. J.* **2016**, *300*, 98–118.

[18] Zhang, X. X.; Wang, Z. C.; Zhou, G. T.; Li, J.; Li, C.; Lin, C.; Xin, X. Z. Multifunctional metamaterials based on MXene composite aerogels for integrated load-bearing and multiphysics wave attenuation. *Compos. Part B: Eng.* **2026**, *309*, 113075.

[19] Worsley, M. A.; Pauzauskie, P. J.; Olson, T. Y.; Biener, J.; Satcher, J. H.; Baumann, T. F. Synthesis of graphene aerogel with high electrical conductivity. *J. Am. Chem. Soc.* **2010**, *132*, 14067–14069.

[20] Wu, Q. L.; Zeng, Z. H.; Xiao, L. From 2D graphene and MXene nanolayers to 3D biomimetic porous composite aerogels for electromagnetic interference shielding. *Compos. Part A: Appl. Sci. Manuf.* **2024**, *177*, 107939.

[21] Pinto, S. C.; Gonçalves, G.; Sandoval, S.; López-Periago, A. M.; Borras, A.; Domingo, C.; Tobias, G.; Duarte, I.; Vicente, R.; Marques, P. A. A. P. Bacterial cellulose/graphene oxide aerogels with enhanced dimensional and thermal stability. *Carbohydr. Polym.* **2020**, *230*, 115598.

[22] Deng, Z. J.; Gao, C. Q.; Feng, S.; Zhang, H. F.; Liu, Y. W.; Zhu, Y.; Wang, J. Z.; Xiang, X.; Xie, H. Y. Corrigendum to "highly compressible, light-weight and robust nitrogen-doped graphene composite aerogel for sensitive pressure sensors" [Chem. Eng. J. 471 (2023) 144790]. *Chem. Eng. J.* **2025**, *505*, 159648.

[23] Yu, Z.; Dai, T. W.; Yuan, S. W.; Zou, H. W.; Liu, P. B.

Electromagnetic interference shielding performance of anisotropic polyimide/graphene composite aerogels. *ACS Appl. Mater. Interfaces* **2020**, *12*, 30990–31001.
[24] Xie, Y. S.; Han, M.; Wang, R. D.; Zobeiri, H.; Deng, X.; Zhang, P. X.; Wang, X. W. Graphene aerogel based bolometer for ultrasensitive sensing from ultraviolet to far-infrared. *ACS Nano* **2019**, *13*, 5385–5396.
[25] Wei, H. G.; Li, A.; Kong, D. S.; Li, Z. Z.; Cui, D. P.; Li, T.; Dong, B. B.; Guo, Z. H. Polypyrrole/reduced graphene aerogel film for wearable piezoresisitic sensors with high sensing performances. *Adv. Compos. Hybrid Mater.* **2021**, *4*, 86–95.
[26] Yang, G. H.; Zhang, X. F.; Wang, R. J.; Liu, X.; Zhang, J. M.; Zong, L.; Yang, H. S. Ultra-stretchable graphene aerogels at ultralow temperatures. *Mater. Horiz.* **2023**, *10*, 1865–1874.
[27] Shen, L. L.; Zhu, T. Q.; Shi, L. W.; Zhao, G.; Zhang, W. H.; Jian, X. G.; Xu, J. Dynamic damage evolution and thermal-strain rate coupled modeling of CF/PPESK composites: Synergistic coupling of thermal activation and hysteresis mechanisms. *Compos. Part B: Eng.* **2025**, *307*, 112923.
[28] Zhang, H. Y.; Li, J. Y.; Pan, Y.; Liu, Y. F.; Mahmood, N.; Jian, X. Flexible carbon fiber-based composites for electromagnetic interference shielding. *Rare Met.* **2022**, *41*, 3612–3629.
[29] Illarionov, Y. Y.; Waltl, M.; Rzepa, G.; Kim, J. S.; Kim, S.; Dodabalapur, A.; Akinwande, D.; Grasser, T. Long-term stability and reliability of black phosphorus field-effect transistors. *ACS Nano* **2016**, *10*, 9543–9549.
[30] Chen, K. J.; An, X.; He, T. L.; Jiang, Y. H.; Shen, J. H.; Li, Z. C.; Ma, X. F.; Sun, Q. F.; Zheng, J. J.; Chen, Y. M. Multi-component collaborative design yields robust hydrogel sensors with superior environmental adaptability for machine learning-assisted gesture recognition. *J. Colloid Interface Sci.* **2026**, *702*, 138953.
[31] Xia, Y.; Wang, Q. Y.; Liu, Y. L.; Zhang, J.; Xia, X. H.; Huang, H.; Gan, Y. P.; He, X. P.; Xiao, Z.; Zhang, W. K. Three-dimensional polyimide nanofiber framework reinforced polymer electrolyte for all-solid-state lithium metal battery. *J. Colloid Interface Sci.* **2023**, *638*, 908–917.
[32] Yue, J. W.; Qin, M. M.; Yu, H. T.; He, Q. X.; Feng, W. Superelastic graphene-based composite aerogel for thermal and electromagnetic protection in extreme temperature environments. *Adv. Funct. Mater.* **2025**, *35*, 2508319.
[33] Zhang, J.; Peng, H. L.; Zhang, H.; Maruyama, S.; Lin, L. The roadmap of graphene: From fundamental research to broad applications. *Adv. Funct. Mater.* **2022**, *32*, 2208378.
[34] Zhang, Y.; Xu, M. K.; Wang, Z. G.; Zhao, T. Y.; Liu, L. X.; Zhang, H. B.; Yu, Z. Z. Strong and conductive reduced graphene oxide-MXene porous films for efficient electromagnetic interference shielding. *Nano Res.* **2022**, *15*, 4916–4924.
[35] Ou, H. Y.; Feng, S.; Liu, Z. H.; Xiang, X. Polydopamine surface modification facilitates high specific capacitance in reduced graphene oxide aerogel. *Chem. Eng. J.* **2025**, *512*, 162361.
[36] Cai, W. R.; Ma, W. J.; Chen, W. H.; Liu, P. J.; Liu, Y. S.; Liu, Z. X.; He, W.; Li, J. J. Microwave-assisted reduction and sintering to construct hybrid networks of reduced graphene oxide and MXene for electromagnetic interference shielding. *Compos. Part A: Appl. Sci. Manuf.* **2022**, *157*, 106928.
[37] Cheng, Z.; Wang, R. F.; Cao, Y. S.; Cai, Z. H.; Zhang, Z. W.; Huang, Y. Intelligent off/on switchable microwave absorption performance of reduced graphene oxide/VO_2 composite aerogel. *Adv. Funct. Mater.* **2022**, *32*, 2205160.
[38] Wang, J. J.; Jing, G. G.; Zheng, R. J.; Huang, Z. J.; Sun, W.; Gao, Z. Y. Ethylenediamine tetramethylenephosphonic acid as a selective collector for the improved separation of chalcopyrite against pyrite at low alkalinity. *Int. J. Min. Sci. Technol.* **2023**, *33*, 873–882.
[39] Zhu, Z. W.; Zhan, L. J.; Shih, T. M.; Wan, W.; Lu, J.; Huang, J. J.; Guo, S. S.; Zhou, Y. H.; Cai, W. W. Critical annealing temperature for stacking orientation of bilayer graphene. *Small* **2018**, *14*, 1802498.
[40] Chen, H. D.; Liu, X. H.; Zhang, S. Q.; Xu, S. M.; Fu, T.; Wang, Y. Z. Full recovery of polyimide wastes into high-value products through break and reconstruction of imide ring. *Adv. Sci.* **2025**, *12*, 2414416.
[41] Yu, Y.; Zhuang, Z. H.; Zhang, W. J.; Xue, T.; Wang, C. X.; Yin, Y. J. Cellulose-based aerogel fibers with enhanced mechanical properties for thermal insulation and humidity response. *Int. J. Biol. Macromol.* **2025**, *323*, 147053.
[42] Xu, Y. X.; Sheng, K. X.; Li, C.; Shi, G. Q. Self-assembled graphene hydrogel via a one-step hydrothermal process. *ACS Nano* **2010**, *4*, 4324–4330.
[43] Jia, G. E.; Yue, X. Y.; Duan, L. M. H.; Yin, R.; Pan, C. F.; Liu, H.; Liu, C. T.; Shen, C. Y. Biomimetic gradient fibrous aerogel pressure sensor featuring ultrawide sensitive range and extraordinary pressure resolution for machine learning enabled posture recognition. *Adv. Fiber Mater.* **2025**, *7*, 1632–1647.
[44] Zhang, M. Y.; Liu, S.; Liu, S.; Jia, G. E.; Zhan, P. F.; Liu, C. T.; Shen, C. Y.; Liu, H. Multi-layered gradient-structured TPU/CNTs aerogel with ultra-wide pressure detection capabilities for machine learning-assisted fruit recognition. *Adv. Compos. Hybrid Mater.* **2025**, *8*, 79.
[45] Zhang, K. Q.; You, H. B.; Liu, Y. X.; Lin, F. L.; Li, Y. N.; Jia, L. N.; Bao, J. X.; Ge, X.; Pan, G. F.; Yu, H. T. et al. Development of a multifunctional and biocompatible hydrogel for flexible implantable sensors. *Chem. Eng. J.* **2025**, *522*, 167403.
[46] Zhang, K. Q.; Yao, T. T.; Zhao, D.; Li, Y. N.; Yu, H. T.; Jia, L. N.; Xing, R. G. Multifunctional graphene-containing hydrogel flexible strain sensor for intelligent sign language recognition and human motion detection. *Nano Res.* **2026**, *19*, 94908664.
[47] Jin, H. H.; Yu, R. H.; Hu, C. X.; Ji, P. X.; Ma, Q. L.; Liu, B. S.; He, D. P.; Mu, S. C. Size-controlled engineering of cobalt metal catalysts through a coordination effect for oxygen electrocatalysis. *Appl. Catal. B: Environ.* **2022**, *317*, 121766.
[48] Cudjoe, E.; Khani, S.; Way, A. E.; Hore, M. J. A.; Maia, J.; Rowan, S. J. Biomimetic reversible heat-stiffening polymer nanocomposites. *ACS Cent. Sci.* **2017**, *3*, 886–894.
[49] Zhong, A.; Li, J. H.; Zhang, Y.; Zhang, F.; Wang, T.; Zhang, G. P.; Sun, R.; Wong, C. P. Low temperature microwave fabrication of three-dimensional graphene/polyimide foams with flexibility strain responsivity. *Compos. Part A: Appl. Sci. Manuf.* **2020**, *137*, 105995.
[50] Ding, Q. L.; Wang, H.; Zhou, Z. J.; Wu, Z. X.; Tao, K.; Gui, X. C.; Liu, C.; Shi, W. X.; Wu, J. Stretchable, self-healable, and breathable biomimetic iontronics with superior humidity-sensing performance for wireless respiration monitoring. *SmartMat* **2023**, *4*, e1147.
[51] Sinterhauf, A.; Traeger, G. A.; Pakdehi, D. M.; Schädlich, P.; Willke, P.; Speck, F.; Seyller, T.; Tegenkamp, C.; Pierz, K.; Schumacher, H. W. et al. Substrate induced nanoscale resistance variation in epitaxial graphene. *Nat. Commun.* **2020**, *11*, 555.
[52] Zeng, Z. H.; Wu, N.; Yang, W. D.; Xu, H.; Liao, Y. Z.; Li, C. W.; Luković, M.; Yang, Y. F.; Zhao, S. Y.; Su, Z. Q. et al. Sustainable-macromolecule-assisted preparation of cross-linked, ultralight, flexible graphene aerogel sensors toward low-frequency strain/pressure to high-frequency vibration sensing. *Small* **2022**, *18*, 2202047.
[53] Jiang, M. Z.; Li, B.; Zhao, Y. H.; Mo, W. X.; Peng, Z. Y.; Wang, W. H.; Liao, F. X. Superelastic biomass-based carbon aerogels reinforced by vein-like networks and pillar structures for piezoresistive sensing, high-temperature applications, and supercapacitors. *Adv. Funct. Mater.* **2026**, *36*, e13514.
[54] Zhao, Y. H.; Chen, H. M.; Qiao, S. Y.; Wang, Z.; Yan, J. L. Hierarchically porous polyimide/graphene aerogels with superior compressibility and electromagnetic interference shielding performance. *J. Mater. Chem. A* **2025**, *13*, 22613–22620.